STORY STORY

Contents lists available at ScienceDirect

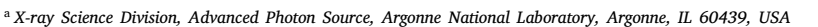
Nuclear Inst. and Methods in Physics Research, A

journal homepage: www.elsevier.com/locate/nima



Extended range X-ray pair distribution functions

C.J. Benmore ^{a,*}, O.L.G. Alderman ^b, D. Robinson ^a, G. Jennings ^a, A. Tamalonis ^b, J. Ilavsky ^a, E. Clark ^b, E. Soignard ^c, J.L. Yarger ^c, J.K.R. Weber ^{a,b}



b Materials Development, Inc., Arlington Heights, IL 60004, USA

ARTICLE INFO

Keywords: Pair distribution function X-ray diffraction Small angle scattering Wide angle scattering Pair distance distribution function Disordered materials

ABSTRACT

Here we describe a dual detector system for high-energy X-ray, simultaneous, small and wide-angle X-ray scattering (SAXS and WAXS), designed to extract extended-range pair distribution functions (ER-PDF) for disordered materials. The hardware and software provides continuous reciprocal space coverage over atomic to nanometer length-scales. Details of the varying resolution, splicing of data and normalization on an absolute scale are outlined. In addition, the combination of SAXS and WAXS theory is considered with a view to enabling a direct Fourier transformation of the structure factor spanning multiple length-scales into real space. Important distinctions between the ER-PDF and the pair distance distribution function (PDDF) representations are demonstrated. It is shown that when the SAXS intensity in the structure factor, S(Q), is similar to the WAXS intensity, the contributions to the ER-PDF are minimal. However, when the SAXS S(Q) intensities are substantially stronger than the WAXS, the ER-PDF can provide important structural information on the local, intermediate and nanometer length-scales. Notably, the ER-PDF method provides direct information on particle sizes and their density distributions, overcoming the limitations of PDDF analysis for densely packed systems.

1. Introduction

Simultaneous high-energy small and wide-angle X-ray scattering (SAXS and WAXS) instrumentation and methods are described with a view to performing Extended Range (atomic) Pair Distribution Function (ER-PDF) measurements out to a few hundred Angstroms. High energy X-rays (>50 keV) provide a bulk probe of the sample structure, especially in extreme environments, rather than a near-surface measurement more typical of grazing incidence SAXS. While the goal of making continuous momentum transfer Q coverage measurements from small to wide angles for PDF has previously been realized in a time-offlight neutron instrument [1,2], to our knowledge there has only been one report on an extended range X-ray PDF measurement [3]. Although more conventional SAXS-WAXS techniques have been implemented using lower-energy X-rays, these are typically analyzed in reciprocal space [4-8]. A pre-requisite of combining SAXS and WAXS methods for PDF analysis, is that there is no gap in Q-space between the small and wide-angle ranges, which would lead to missing data in the direct Sine Fourier transformation of the measured structure factor into real space. Extracting extended range PDF's as described in this work is important for the investigation of the order and disorder in materials up to length scales of a few tens of nanometers, which is not readily accessible using standard crystallographic techniques.

The primary motivation for this work is the structural investigation of heterogeneous disordered materials, which are commonly encountered in, for example; crystallization from the liquid state [9], the formation of glasses, amorphous materials [10], nanomaterials [11,12], and in liquid crystal formation in pharmaceuticals [13] among others. The pair distribution function obtained from WAXS measurements is an essential tool in studying atomic structural order and disorder through the direct Sine Fourier transform of the total structure factor into real space. A recent review of the applications of this technique using highenergy X-ray diffraction to attain high-quality, high-resolution data has been given by Benmore [14]. Equally, the application of SAXS is widespread in investigating the size and shape of groups of atoms or molecules covering a vast range of length-scales, including the nanoscale, and density fluctuations in soft matter etc. [15–17].

We provide a brief review of SAXS and PDF theory which points towards ways of bridging the two techniques and a rationale for the optimum representations in real space. This brings into focus considerations of resolution and normalization procedures. Moreover, we address the question of when it is worthwhile to extract an ER-PDF and when structural information can be more readily observed in reciprocal space. The instrumentation and software comprises of permanently mounted SAXS and WAXS detectors that enables simultaneous SAXS—WAXS measurements over a wide and continuous Q-range and temporal resolution on sub-second timescales.

E-mail address: benmore@anl.gov (C.J. Benmore).

^c Arizona State University, Tempe, AZ 85287, USA

Corresponding author.

2. Theoretical considerations

Wide angle measurements contain both Bragg and diffuse scattering, representative of both long- and short-range order respectively, and are associated with (the electron clouds surrounding) atoms, their connectivity and spatial arrangements. For atomic pair distribution functions, the maximum Q value, Q_{max} , defines the structural resolution in real space. The best real-space resolution is obtained without using a window function (effectively a step window function that is unity up to Q_{max} and zero beyond) which yields a FWHM [18], Δr_{step} = $3.791/Q_{\text{max}}$. Therefore, a large value of Q_{max} is important for determining accurate bond lengths and local structural arrangements. The use of high X-ray energies > 50 keV is essential for accessing high momentum transfers and achieving the highest resolution in real space. Conversely, to measure ordering on longer length-scales it is necessary to access low Q-values, whereby $Q = 2\pi/r$ provides information on density fluctuations up to a distance r in real space. Porod's law addresses scattering in the intermediate region where momentum transfers are small, typically $Q \lesssim 0.1 \text{ Å}^{-1}$, compared to usual Bragg diffraction, but are larger than the Guinier region typically associated with information on the size and shape of particles.

This raises the important issue of how far out in real space a standard PDF experiment, measured over a typical WAXS Q-range, can provide meaningful structural information. Salmon et al. [19] have shown that for a PDF measurement on glass with $Q_{\rm min} \sim 0.5 ~{\rm \AA}^{-1}$ (corresponding to r $\sim 2~\pi/0.5 = 12.6~{\rm \AA}$) real space oscillations can still be observed beyond 60 Å, where the correlation length, $2\pi/4Q$, is governed by the FWHM (4Q) of the principal peak. For systems that have no significant SAXS signal this is a perfectly reasonable result since the low-Q region contributes very little to the Fourier transform from reciprocal to real space [20]. However, for systems that have nanoscale density fluctuations the effect of $Q_{\rm min}$ on the PDF can be significant [12] and these are the cases considered here.

For a material comprising an arrangement of mesoscopic particles the small angle scattering signal in the Porod region can be understood in terms of correlations between different interfaces. For random interparticle correlations the scattering in this region is dominated by the local surface roughness, such that the differential scattering cross section for homogeneous particles with smooth interfaces follows a power law known as Porod's law e.g. [15]. For the limiting case, in the tail of the SAXS curve for $Q \cdot r > 10$, the scattered electron intensity, I(Q), can be written as,

$$\lim_{Q \to \infty} \frac{d\sigma}{dQ} = I(Q) = 2\pi |\Delta\rho|^2 S_V Q^{-4}$$
(1)

where S_V is the surface area of the particles per unit volume of irradiated sample $V_{\rm P}$, and the *scattering contrast* between the scattering particles $\rho_{\rm S}$, and their surroundings $\rho_{\rm m}$, is given by,

$$\left|\Delta\rho^{2}\right| = \left|\rho_{s} - \rho_{m}\right|^{2} = r_{e}^{2} \left\langle f\right\rangle^{2}.\tag{2}$$

 r_e is the scattering length of a single electron given by the Thompson radius. $\langle f \rangle^2$ is the mean square atomic form factor (used to describe the electron cloud distribution) where,

$$\langle f \rangle^2 = \left[\sum_{i=1}^n c_i f_i(Q) \right]^2$$
 and, similarly $\langle f^2 \rangle = \sum_{i=1}^n c_i f_i^2(Q)$. (3)

Here i (or j) represent different atomic species in a material of n species. Rougher surfaces will have Q-exponents smaller than 4. In addition to extracting the Porod exponent, $p \lesssim 4$, at low Q-values the shape of particles can be described as a particle form factor. In conventional SAXS experiments the particle form factor, P(Q), can sometimes be expressed as an analytical function and fitted to the measured X-ray intensity. The scattered intensity also contains information on interparticle interactions, described by a particle structure factor, $S_P(Q)$, that tends to unity at high-Q [20].

$$I(Q) = (N/V) V_p^2 |\Delta \rho|^2 P(Q) S_P(Q)$$
(4)

where N/V is the number density of particles.

An important aspect in determining the particle shape for *dilute* systems is the extraction of the pair distance distribution function (PDDF), P(r), which is expressed by the Fourier transform [15,21],

$$P(r) = \frac{1}{2\pi^{2}V_{P}|\Delta\rho|^{2}} \int_{0}^{\infty} Q^{2}I(Q) \frac{\sin(Qr)}{Qr} dQ$$
 (5)

This function starts at zero and shows a distribution of distances arising from correlations within the particle and returns to zero at the largest particle diameter. However, there are serious difficulties using this approximation for hollow or composite particles or densely packed systems.

As mentioned previously, at the atomic level the Fourier transform of I(Q) contains information on the shape of the electron cloud surrounding the nucleus. Using the independent atom approximation, $\langle f \rangle$ is generally assumed to be spherically symmetric in PDF analysis, such that the pseudo-nuclear WAXS structure factor, S(Q) can be extracted through [11,22,23],

$$\frac{1}{N}\frac{d\sigma}{d\Omega} = \frac{I(Q)}{N} = \langle f \rangle^2 \left[S(Q) - 1 \right] + \langle f^2 \rangle \tag{6}$$

where N is the number of atoms. The measured S(Q) is most commonly expressed using the Faber–Ziman formalism [24] as the sum of the X-ray weighted element specific partial structure factors $S_{ij}(Q)$,

$$S(Q) - 1 = \left(\frac{\sum_{i,j} c_i c_j f_i(Q) f_j(Q) \left[S_{ij}(Q) - 1\right]}{\langle f \rangle^2}\right)$$

$$\tag{7}$$

The inversion of the WAXS total structure factor S(Q) to the atomic differential pair distribution function, D(r), is obtained using the Hannon–Howells–Soper nomenclature [23,25,26],

$$D(r) = \frac{2}{\pi} \int_{Q_{\text{min}}}^{Q_{\text{max}}} Q[S(Q) - 1] \sin(Qr) dQ.$$
 (8)

D(r) is a convenient representation to use for extended range PDF measurements because it removes the bulk density contribution and emphasizes the larger-r part of the transform compared to the standard representation of the atomic pair distribution function, G(r),

$$D(r) = 4\pi \rho_0 r [G(r) - 1]$$
(9)

where ρ_0 is the atomic number density in atoms/Å [3]. We note that ρ_0 commonly used in PDF literature has a different meaning to ρ_S and ρ_m used in SAXS literature to describe the scattering density and contrast.

Here, we merge the SAXS and WAXS signals at the differential cross section, I(Q), level and convert to the atom–atom function D(r) using Eqs. (6) through (8). In practice the contribution of intense SAXS signals in S(Q), originating from P(Q) or $S_P(Q)$, can create Fourier transform artifacts in the real space D(r) function [1] and remains an inherent problem. This is because the rapidly rising Porod signals are abruptly truncated at $Q=Q_{\min}$, transforming into a long wavelength oscillation in real space. In addition, the separation of the real space contribution of the particle form factor from the structural component describing the pair interactions can often be problematic for complex geometries.

3. Hardware and layout

Here we describe high energy X-ray instrumentation designed to enable simultaneous SAXS and WAXS detector measurements, with a continuous Q coverage over the nominal range ~ 0.03 to ~ 20 Å $^{-1}$ and an overlap of $\Delta Q \sim 1.5$ Å $^{-1}$, using monochromatic X-rays in the range 60–80 keV. The wide overlap range between the SAXS and WAXS datasets means that both will cover the region of the so-called *first sharp diffraction peak* often observed in glasses and amorphous materials with intermediate range order [27], the layer spacing in clays and cements [28], features in scattering from biomaterials [29] and internanoparticle interactions [12]. The goal here is to allow a combination and normalization of the small and wide-angle data to enable a detailed interpretation of the results in both reciprocal and real space. A

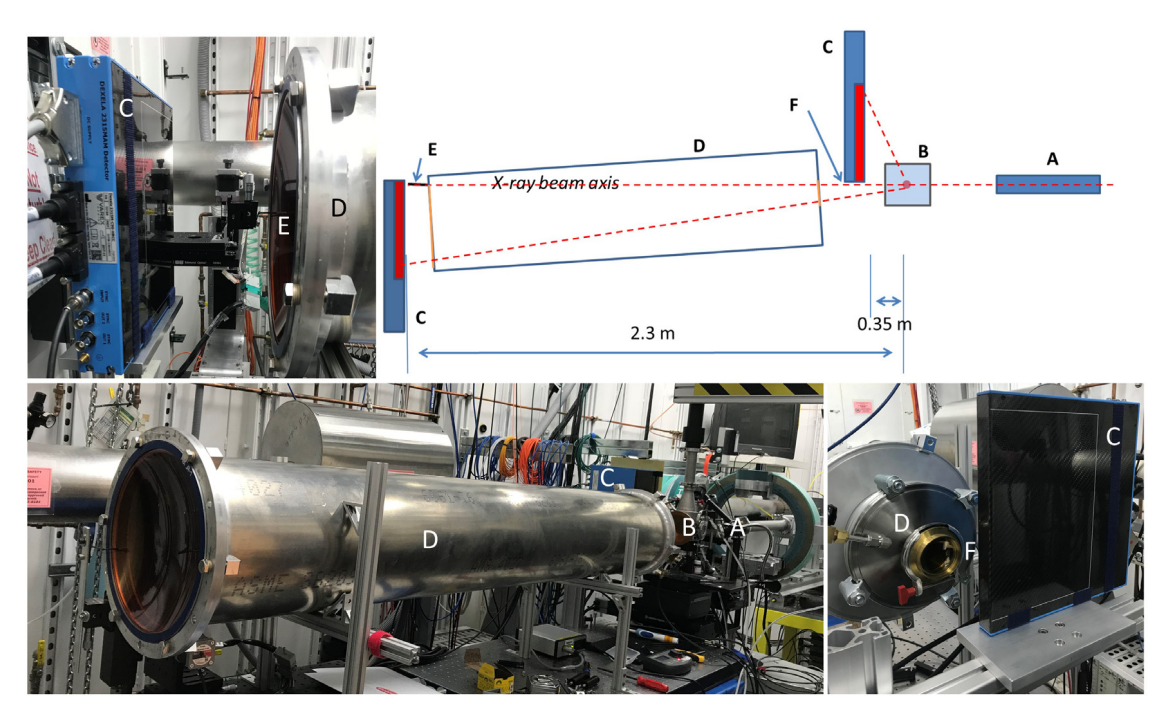


Fig. 1. Top. Schematic layout of a typical high-energy simultaneous SAXS–WAXS set up. (A) X-ray beam conditioning optics; (B) sample and sample environment; (C) Dexela 2315-MAM detectors; (D) evacuated tube with Kapton windows; (E) chamfered tungsten beamstop on carbon fiber rod which is positioned up against the curved downstream Kapton window using an adjustable stage; (F) a 3 mm offset at edge of detector active area. Photographs from left to right: Downstream SAXS detector positioned behind beamstop (top). Large section of evacuated tube with Kapton windows. WAXS detector with upstream window of evacuated tube in background.

schematic diagram and photographs of the simultaneous SAXS–WAXS set-up in the 6-ID-D station at the Advanced Photon Source are shown in Fig. 1.

Beamline 6-ID-D provides monochromatic X-rays over an energy range from 50–130 keV (wavelengths from ~0.248–0.095 Å). Typically, 60 keV X-rays provide sufficient penetrating power to probe the bulk structure of the sample and a large Q range with extension into the Porod regime. Length scales from $2\pi/Q_{\rm max} \sim 0.3$ to $2\pi/Q_{\rm min} \sim 200$ Å are accessed, with wider ranges accessible using larger detector separation distance, at the expense of Q-space overlap. The incoming monochromatic high-energy beam is collimated by 3 pairs of slit blades and a pinhole. The first slit package close to where the beam enters the hutch is used to define the beam size and shape. The third downstream optic placed close to the sample is a pinhole in a 0.5 mm thick tungsten foil, followed by a clean-up slit just in front of the sample. Careful alignment of all the optics is required to ensure slit scatter is not present in either the SAXS or WAXS signal. This is especially important for high-energy X-ray total scattering PDF measurements where precise background subtraction and instrumental corrections are essential [30] for placing the data on an absolute scale.

The instrument is built around the use of two Dexela 2315-MAM (mammography) detectors, one each in the SAXS and WAXS positions. This WAXS detector was chosen primarily because the X-ray sensor area is located only 2.75 mm from one edge of the detector housing, allowing significant angular overlap between detectors permanently mounted at the SAXS and WAXS positions. The detectors have a high resolution CsI scintillator with an active area of 230 mm \times 145 mm and square 74.8 µm pixels. The SAXS detector type was chosen to be the same as the WAXS detector to have identical detector characteristics i.e. the same detector efficiencies to aid in the merging procedure, and for simplifying the simultaneous data acquisition needed for the time resolved measurements. The standard MAM detector provides 26 frames per second. An important consideration is the non-linear response of the CMOS detector over the dynamic range of the detector. To investigate this for high energy X-rays, the measured count rate is shown as a function of incident flux in Fig. 2. Although for most of the samples studied the scattered intensities were comparable in

both the SAXS and the WAXS detectors (e.g. see Fig. 3), the variation within a single detector can vary by a few orders of magnitude. The detector non-linearity is most pronounced at low count rates, and this is particularly relevant at high Q-values e.g. the atomic form factor leads to a decrease by an order of magnitude in the measured WAXS signal from SiO_2 . To investigate the effect of non-linear detector response on S(Q) we have compared the WAXS signal from SBA-15 measured using the Dexela 2315-MAM detector, to the WAXS signal from glassy SiO_2 measured using a single-photon counting Pilatus 2M CdTe detector. The results show that despite the non-linearity there are only minor effects on the normalization or distortion of S(Q).

Flat field measurements of the Dexela 2315 MAM detectors were performed at 100 keV using W and Pb samples with the detectors positioned at two different distances, at an angle of 90 degrees to the incident beam. The X-ray intensities were processed using Fit2D [31] by removing smoothly varying geometrical effects and flat field maps were created using imageJ [32]. Both the W and Pb samples measured at different distances yielded the same results. Horizontal and vertical streaks and lines from manufacture were completely removed in the subsequent analysis of the SAXS-WAXS data, however slight differences in adjacent panels were observed to vary over second timescales and could not be removed. At the current time this variation in low-level noise (within the specifications of the detector) is the limiting factor for the high-Q limit, $Q_{\rm max}$, in the WAXS detector for weakly scattering samples. The tube between the SAXS and WAXS detectors was evacuated to a pressure of ~10 Torr and a 2 mm diameter chamfered tungsten beamstop positioned touching the deformed thin downstream Kapton window. If the beamstop was further downstream a substantial increase in background from the window was observed in the SAXS detector.

4. Data acquisition and software

QXRD is an application designed to control the readout of amorphous silicon flat panel X-ray detectors made by Perkin Elmer and Varex [33]. The software acts as a bridge between the dynamic link library provided by Perkin Elmer and the APS beamline data acquisition

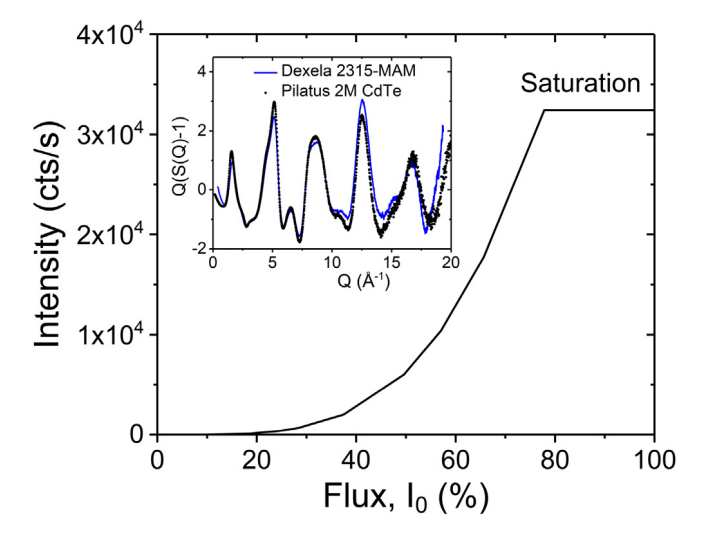


Fig. 2. Count rate as a function of incident flux for the Dexela 2315-MAM detector measured using 60 keV X-rays, showing non-linear behavior at low count rates. The insert shows the effect on the total structure factor, where the WAXS S(Q) for SBA-15 measured using the Dexela 2315-MAM detector (blue line) is compared to the WAXS S(Q) for glassy SiO_2 measured using a single-photon counting Pilatus 2M CdTe detector (black circles). (For interpretation of the references to color in this figure legend, the reader is referred to the web version of this article.)

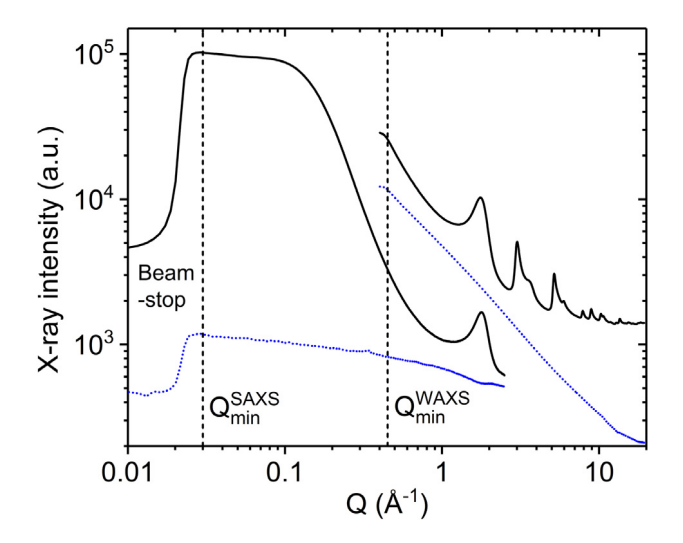


Fig. 3. The measured X-ray intensity for glassy carbon (black line) and the background from air scattering (blue dotted line) in the SAXS and WAXS detectors. The minimum usable Q-values are marked as dashed lines; Q_{min}^{WAXS} is defined by the distance from the beam to the nearest active detector pixels and Q_{min}^{SAXS} is determined by the start of the attenuation of the signal by the beamstop.

software *spec* [34]. It also provides a convenient GUI interface to the detector. Dark images are recorded at least every 20–30 min during routine operation to avoid any effects from electronic drift caused by temperature or other fluctuations.

The dual SAXS-WAXS system described here simultaneously records images from both detectors to provide information on atomistic through mesoscopic length-scales. This is particularly useful for performing time-resolved measurements during phase transitions and chemical reactions etc. Fast measurements require that three conditions are met in the execution of the experiments: (i) sufficient X-ray flux to achieve adequate signal to noise in the data, (ii) adequate detector response to acquire the data with time resolution needed to observe the transition, and (iii) adequate control of the process to synchronize the data. Data collection can be synchronized with external equipment via a trigger

signal. Previous examples of this feature for WAXS have already been reported [35,36].

5. Data analysis

The WAXS detector signal was calibrated using NIST standard CeO₂ and the SAXS detector calibrated using silver behenate to determine the precise sample to detector distances together with detector orientation angles. Both data sets were analyzed using the Fit2D software [31] and corrected for polarization, rotation and tilt. The program PDFgetX2 [11] was used to correct the WAXS sample signal for background, oblique incidence, absorption and detector efficiency effects [30] for all but one of the data sets presented here. GudrunX [37] was used for an equivalent analysis of the ZIF-62 glass. The oblique incidence correction accounts for the increase in measured intensity due to the longer effective thickness of the scintillator at oblique angles, while a parallax effect results a shift in peak position due to highenergy photons traversing several pixels before being detected. The oblique incidence correction is calculated and fixed in the analysis (see Skinner et al. [30]). The parallax issue is a minor effect and Marlton et al. [38] have shown the magnitude of the parallax on the PDF is ~0.15% for 103keV X-rays at a sample to detector distance of 351 mm. The effect in our experiments are expected to be less since we are using incident energies ranging from 60-80keV. Both effects are most apparent at large angles and are not used as adjustable parameters in the SAXS/WAXS overlap region. However, applying the correct transmission factor prior to subtracting the background was found to be important in obtaining good agreement between SAXS and WAXS in the overlap region, where signal-to-background ratio is typically at its lowest (Fig. 3). PDFgetX2 also normalizes to the sample self-scattering and the background corrected SAXS intensity was subsequently normalized to the WAXS data in the Q-space overlap region.

5.1. Combining SAXS-WAXS data

The SAXS–WAXS data are merged to provide a continuous SAXS–WAXS signal covering the entire measured Q-range. The choice of splicing-point in the overlap region between SAXS and WAXS data sets depended entirely on the sample scattering, but was typically determined by the quality of the SAXS data which often became noisy for $Q \gtrsim 1~\rm \AA^{-1}$ due to the 1/R [2] inverse square law fall off in intensity. The different Q-space resolutions of the SAXS and WAXS signals means that any sharp features in the overlap region are better resolved in the SAXS signal, and the WAXS data should be discarded wherever the resolution results in disagreement. If only broad, smooth, features exist in the overlap region, the better statistics associated with the WAXS signal can be utilized. The relative measured resolutions of the SAXS and WAXS detector set ups are shown in Fig. 4 based on the FWHM of the calibration standards.

The SAXS resolution given by ΔQ is found to be essentially constant and is governed by the pixel size, the source-to-sample and the sampleto-detector distances, with the FWHM of the peaks ~6 times narrower than those in the WAXS. The WAXS resolution is governed by the same factors at low $Q (\lesssim 5 \text{ Å}^{-1})$, but at high-Q the larger scattering angles and the shorter sample-to-detector distance leads to significant geometric effects (i.e. oblique incidence, assuming a $\cos^3(2\theta)$ dependence) when using a flat plate detector perpendicular to the incoming beam [30,39]. The disparity in SAXS/WAXS resolution presents an issue similar to that of combining data from different resolution detectors in time of flight neutron PDF measurements [25] and is especially problematic if there is no agreement in the detector overlap region. However, for most disordered materials the scattered X-ray intensity results in only a few broad peaks at low-Q, if any, and the instrument design outlined has left an ample overlap region between detectors to find a suitable splicing point, e.g. see Figs. 5 and 6.

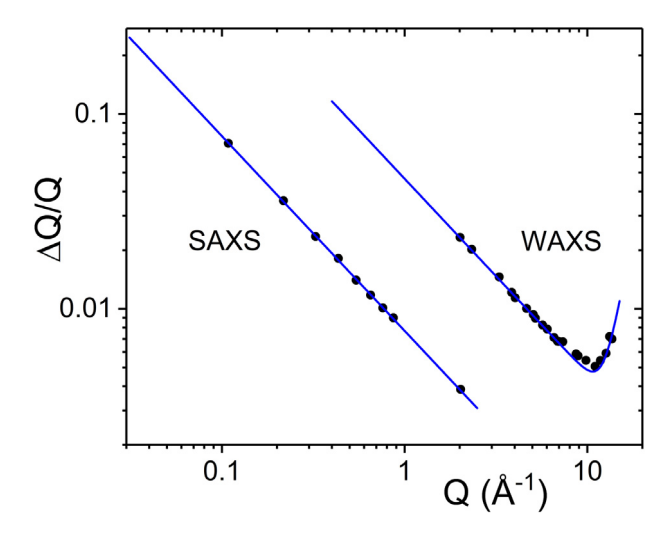


Fig. 4. The measured resolution function (FWHM, ΔQ) based on the calibration standards CeO $_2$ (WAXS, neglecting strain effects) and Ag-Behenate (SAXS) using sample-to-detector distances of 28 cm and 228.8 cm and an incident wavelength of 0.154552 Å. The circles represent the measured FWHM of calibrant peaks best-fitted with Gaussian functions and the lines represent fits based on expected geometrical effects [30].

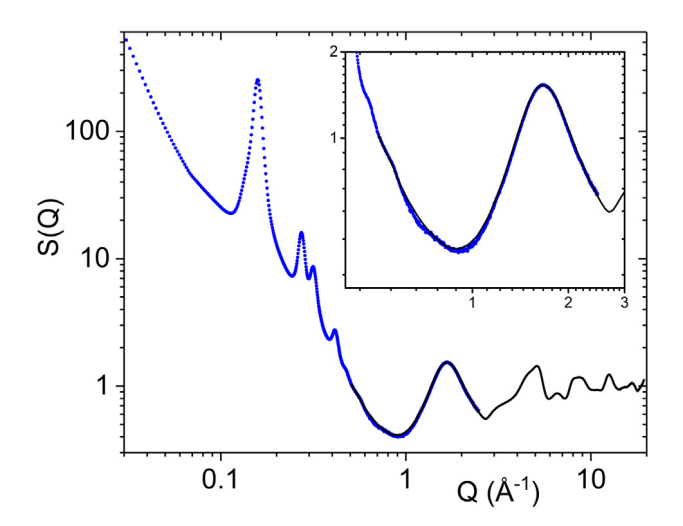


Fig. 5. The overlap region in Q-space between the SAXS and WAXS detectors shown for the case of ordered mesoporous amorphous silica MCM-41.

5.2. Absolute normalization

SAXS and WAXS are conventionally normalized onto absolute intensity scales in different ways. The absolute calibration of small angle scattering data is usually carried out in terms of the differential cross section per unit volume per solid angle [40] and has units of cm⁻¹. Although uncalibrated data can provide meaningful information, absolute normalization can provide quantitative parameters such as the particle number density. Glassy carbon is commonly used as a SAXS intensity calibration standard [41] because of its homogeneous microstructure and durability, although there is some variability between samples. Conversely, WAXS data is normalized to the self-scattering based on the composition weighted atomic form factor(s) $\langle f^2 \rangle$ and Compton scattering at high-Q, typically in the region $>10 \text{ Å}^{-1}$, in terms of electron units. A comparison of the same glassy carbon sample measured on a dedicated SAXS instrument and the SAXS-WAXS instrumentation described in this paper is shown in Fig. 6. Merging the SAXS-WAXS data and placing it on an absolute scale yields an extended atomic structure factor, S(Q).

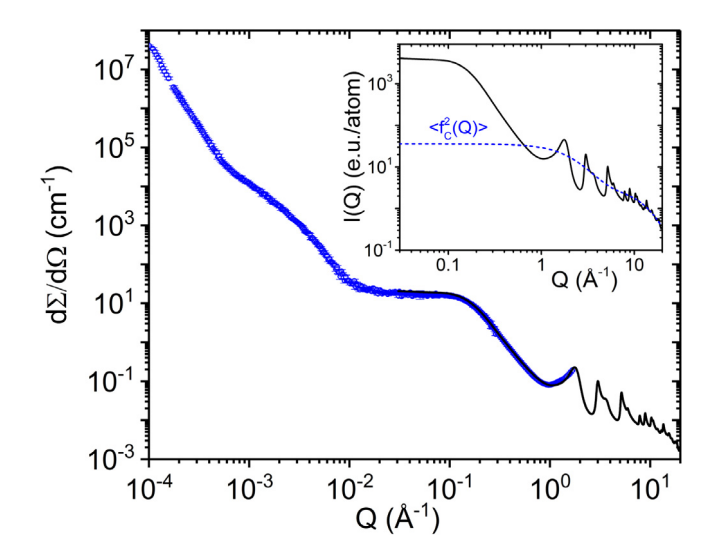


Fig. 6. The SAXS differential cross section for glassy carbon measured on beamline 9-ID (blue circles) compared to the same sample measured on beamline 6-ID-D (black line) using the SAXS–WAXS set-up described here. The insert shows the glassy carbon normalized to the self-scattering at high-Q. The conversion factor between the SAXS differential cross section in cm⁻¹ and the WAXS in electron units for this sample was $N_P V_P^2 r_e^2 / N = 0.005 \, \mathrm{cm}^{-1}$.

5.3. Fourier transformation

If we consider Eq. (8) it can be seen that D(r) is obtained by integrating $Q(S(Q)-1)\sin Qr$ between finite values of Q_{min} and Q_{max} . The minimum Q-value, Q_{min} , is determined by the observable absorption of the SAXS signal by the tungsten beamstop. The maximum Q-value, Q_{max} , is chosen as the highest possible Q-point where the observed oscillations in S(Q) equal to unity (preferably located at a node at $Q>15~{\rm \AA}^{-1}$ to ensure reasonable r-space resolution and minimize spurious ripples from convolution with a sinc-function, arising from Fourier transforming the effective Q_{max} step function [42]). The resulting combined SAXS–WAXS structure factors are binned on two different linear scales either side of the splicing point and require a non-linear discrete Fourier transform, which is performed using a Fast Fourier Transform algorithm in MATLAB using custom developed software to obtain the extended range pair distribution function, D(r).

As previously discussed, for atomic pair distribution functions the maximum Q value, $Q_{\rm max}$, defines the structural resolution in real space. The issue with using a step modification function in the direct Fourier transform of scattering data is the appearance of large, sinc-function, termination ripples either side of peaks in the pair-distribution function. In 1969 Lorch [43] developed a modification function $M(Q,\Delta(r))$, and which goes to zero above $Q_{\rm max}$, to suppress these truncation osin in real space and yielding a FWHM resolution $\Delta r = 5.437/Q_{\rm max}$ [18,37]. Recently other modification functions with varying degrees of broadening have also been investigated [42]. Here we used a modification function of the type previously reported by Skinner et al. for water [44] based on that suggested by Soper and Barney [42], where a = 2.8 and b = 0.5 Å. So Eq. (8) becomes,

$$D(r) = \frac{2}{\pi} \int_{Q_{\min}}^{Q_{\max}} Q[S(Q) - 1] M(Q, \Delta(r)) dQ$$
 (10)

where,

$$M\left(Q,\Delta\left(r\right)\right) = \frac{\sin\left(Q\Delta\left(r\right)\right)}{O\Delta\left(r\right)},$$

$$\Delta(r) = \frac{\pi}{Q_{\text{max}}} \left[1 - \exp\left(-\left\lceil r - a \right\rceil / b\right) \right] \tag{11}$$

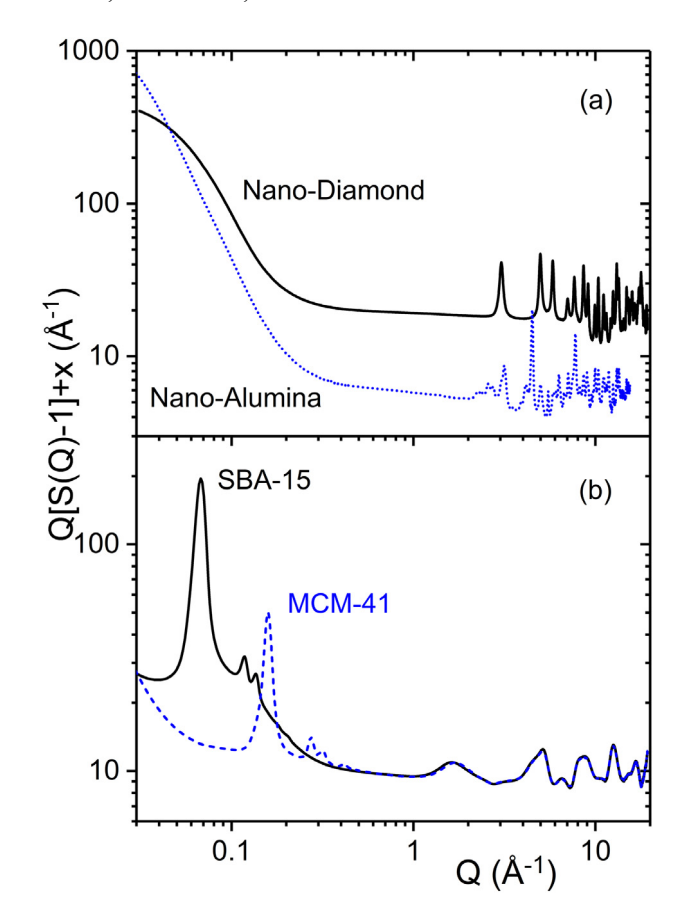


Fig. 7. Extended X-ray structure factors for (a) nano-Diamond (solid line) and nano-Alumina (blue dotted line), offset for clarity and (b) amorphous mesoporous silicas SBA-15 (solid line) and MCM-41 (blue dashed line).

6. Benchmark samples

For many diffraction experiments the combination of SAXS and WAXS reciprocal space data in itself is extremely useful in determining the salient structural features as well as their variation as a function of a thermodynamic parameter such as temperature, pressure or solute concentration or time etc. However, the primary goal here was to investigate the real space manifestation of including the SAXS data in the ER-PDF. Towards this end, a range of samples representative of different types of materials with varying low-Q structural signatures were selected and measured. These included liquid crystals, metalorganic-framework glasses, powdered nano-materials and mesoporous materials.

6.1. Case 1: Nano-materials

The first set of benchmark samples considered were nano-materials that exhibited a continuous rise in SAXS intensity to values substantially larger than the WAXS signal, see Fig. 7(a). For nano-crystalline diamond with a particle size of <100 Å (Sigma-Aldrich, based on TEM) and a density of 3.5 gcm⁻³, the S(Q) displays broadened Bragg peaks and a sharp rise in the Porod region [45]. The associated D(r) in Fig. 8 shows strong oscillatory behavior with the ER-PDF showing the first minimum in D(r) at 96 ± 1 Å corresponding to the average particle size. Similarly, the largest particle diameter obtained from P(r) was found to be 114 Å. Aluminum oxide nanopowder has a 130 Å primary particle size (Sigma-Aldrich, based on TEM). The D(r) indicates the particle size is slightly larger at 145 ± 1 Å, while P(r) yields a much larger value of 185 Å.

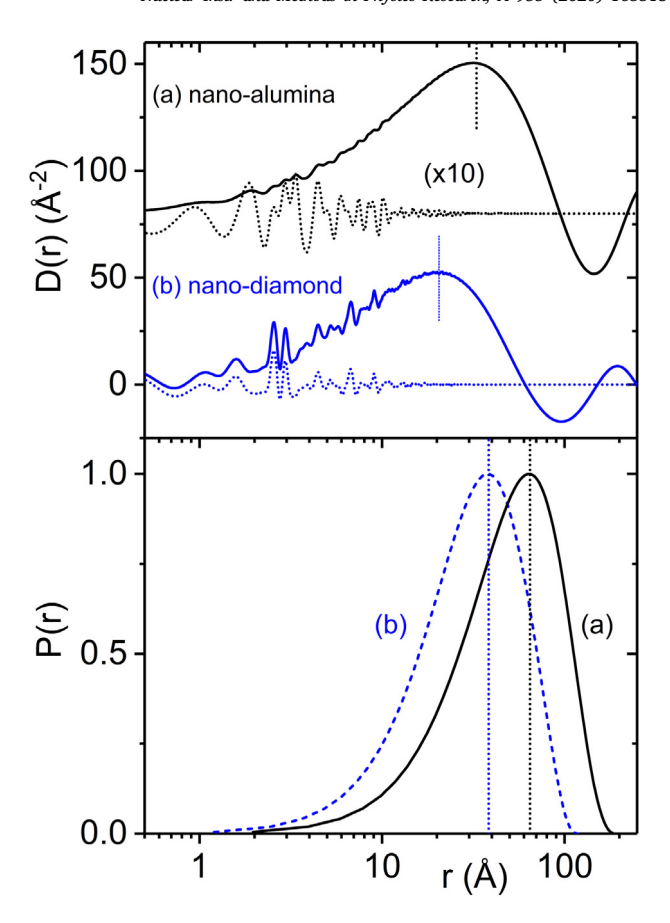


Fig. 8. Top: The SAXS-WAXS extended range X-ray pair distribution functions of (a) nano-Alumina and (b) nano-Diamond (solid lines) compared to the conventional PDF analysis using WAXS data only (dotted lines, note this curve for nano-alumina has been scaled by x10). Bottom: The PDDF for (a) nano-Alumina (solid line) and (b) nano-Diamond (blue dashed line). The maxima are marked by dotted vertical lines.

Furthermore, the conventional WAXS PDF peaks describing the local atom—atom interactions are superimposed on an intense broad peak, which reflects the substantial deviation in local atomic density due to increased number of atom—atom interactions within the core structure of the nanoparticles. The positions of these broad maxima in D(r) are significantly smaller than those observed in the corresponding P(r) functions; 20.5 Å compared to 38.4 Å for nano-diamond and 32.9 Å compared to 64.7 Å for nano-alumina. This is attributed to the effect of inter-particle interactions on accurately extracting the PDDF from densely packed systems [46].

6.2. Case 2: Mesoporous silicas

Secondly, we consider materials with strong peaks in the SAXS regime, Fig. 7(b). Amorphous mesoporous silicas SBA-15 and MCM-41 (Sigma-Aldrich) consist of hexagonal arrays of cylindrical pores with different sizes [47]. The local structure and WAXS signal is dominated by the tetrahedral bonding arrangement of Si by O, characterized by the Si–O, O–O and Si–Si distances. The SAXS region is dominated by the interplanar 100 reflection and smaller 110 and 200 reflections arising from the hexagonally ordered arrangement of cylindrical pores. The D(r) were obtained using nominal densities of ~0.34 gcm⁻³ and found to be dominated by the periodicity arising from the most intense 100 reflection at $Q = 0.159 \text{ Å}^{-1}$ (MCM-41) and $Q = 0.0676 \text{ Å}^{-1}$ (SBA-15) corresponding to periodicities of 40 Å and 93 Å respectively i.e. from maximum to maximum in D(r), Fig. 9.

The high-r oscillations corresponding to the interplanar reflections in MCM-41 are in good agreement with those obtained using neutron

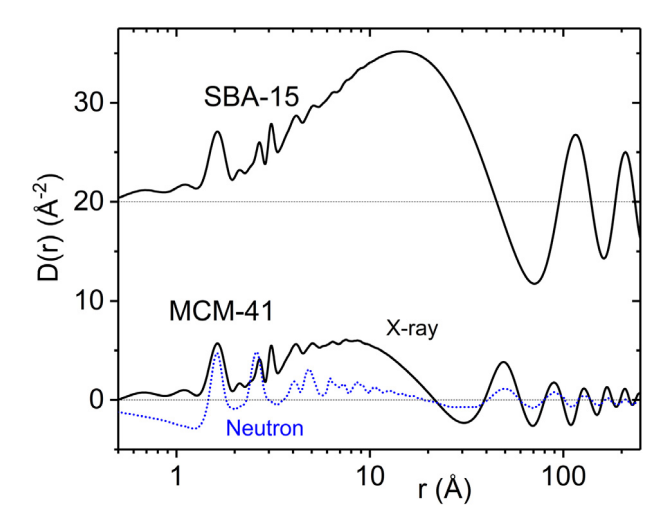


Fig. 9. The extended range X-ray pair distribution functions, D(r), for amorphous mesoporous silicas SBA-15 and MCM-41 (solid black curves). In the lower part of the figure the X-ray MCM-41 is compared to the published neutron pair distribution function for MCM-41 silica from Bowron et al. [1] (blue dotted line, scaled for clarity).

diffraction [1] (see Fig. 9) and qualitatively similar to those published by Kohara et al. [3]. The low-r differences between the X-ray data obtained in this study and the neutron data [1] can be attributed to the different partial atom–atom weighting factors. The larger pore sizes associated with SBA-15 (compared to MCM-41) show much larger density fluctuations as indicated by the stronger 100 reflection.

6.3. Case 3: Low intensity SAXS features

It is clear from Eq. (7) that the factor of Q in the Fourier transform significantly reduces intensities at the lowest Q-values, rendering relatively small SAXS features obscure in the ER-PDF [20]. To investigate when ER-PDF measurements are useful (and when they are not) we also performed extended-range PDF measurements on samples with relatively low SAXS signals. The measured S(Q)'s for itraconazole and ZIF-62 glasses are shown in Fig. 10(a). Their corresponding real space ER-PDF curves are shown in Fig. 10(b).

Itraconazole is a rod-like molecule that can exist in different mesophases that are distinct from its crystal structure. Upon quenching from the melt to room temperature a liquid crystalline lamellar phase can form, within the otherwise long-range disordered glass, characterized by two small but very sharp peaks in the SAXS region [13]. The corresponding D(r) obtained using a density of 1.27 gcm⁻³ is essentially flat for distances >30 Å. The zeolitic imidazolate framework ZIF-62 is an example of a metal-organic framework (MOF) and represents a family of materials where the structural topology and mechanical properties can be chemically tuned. It has recently been shown that ZIF-62 can be melt-quenched to form a glass [48]. Our measurements show SAXS intensity, indicating that some of the porosity inherent to the crystalline phase is retained in the melt and glass. Notably, measurements at different points on the glass gave rise to slightly different SAXS intensities, indicating inhomogeneity of the pore distribution even on the 100s of microns scale (the X-ray beam size was 300 µm square). This could imply that the porosity depends upon the thermobaric history of the melt prior to and during quenching. The ER-PDF obtained using a density = 1.6 gcm^{-3} again shows little structure for r>20 Å. Both this example, and that of glassy itraconazole therefore show no long-range structure in their D(r), and the ER-PDF is essentially the same as the standard PDF obtained using only WAXS data.

These examples demonstrate that as a *rule of thumb* the SAXS S(Q) needs to be an order of magnitude stronger than the WAXS S(Q) to show a significant contribution in the ER-PDF. Of course, there will

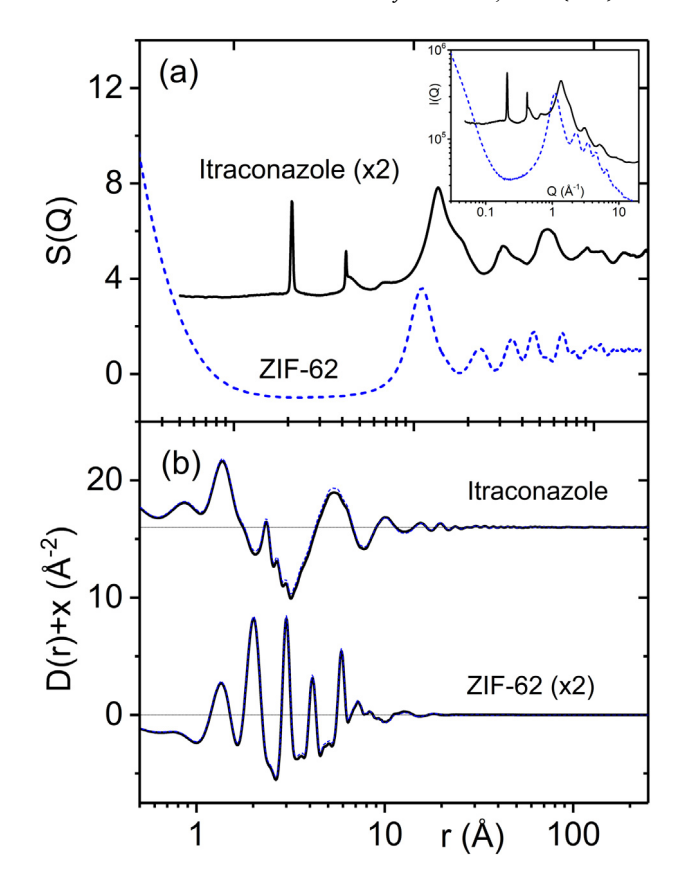


Fig. 10. (a) Extended X-ray structure factors for amorphous itraconazole and ZIF-62 glass (with the corresponding SAXS intensities shown in the insert) and (b) the corresponding extended range pair distribution functions. The solid lines include the entire Q-range and the dotted lines only the WAXS signal. The curves are offset for clarity.

be exceptions to this 'rule' as the details of the Fourier transform will depend on the precise location of the SAXS features compared to the WAXS structure factor.

7. Summary and future directions

This paper describes instrumentation aimed at performing simultaneous high-energy SAXS/WAXS measurements with continuous Qrange coverage, that enables the interrogation of structure from the atomic to the meso-scale through the extraction of extended range pair distribution functions. Although the real space representation contains the same information as the reciprocal space SAXS-WAXS data, it does present some advantages; namely both the local atom-atom correlations and the size and shape of the nanometer-range density distributions are more easily identified. This is particularly useful for characterizing inhomogeneous systems, nanoparticles and mesoporous materials. For systems with strong SAXS signals that are at least an order of magnitude larger than the WAXS signal, ER-PDF is a useful tool in gaining real-space insight into complex systems that can be directly compared to a 3-dimensional atomic scale model. The measured ER-PDFs do not however yield much useful information for systems with weak SAXS signals i.e. where SAXS features are similar in magnitude to the WAXS signal. Most importantly, the ER-PDF is useful for studying concentrated solutions and densely packed nanoparticle systems, where inter-particle interactions affect the SAXS signal used in extracting the geometry of a particle using the pair distance distribution function approach. To investigate this effect further work is in progress to compare the ER-PDF and PDDF for different concentrations of colloidal silica spheres in aqueous solution.

It is anticipated that future versions of this high-energy X-ray technique will be aimed at extending the low-Q limit to include structures on longer length scales. This could be achieved by the use of smaller beams/beam-stops or longer sample-to-detector distances. The latter may require the splicing of spectra from several Q-ranges and careful consideration of overlap ranges and inter-normalization procedures to maintain the data on an absolute scale. Potential applications of the emerging ER-PDF technique include investigation of phase separation and crystallization in glasses and liquids, phase selection in crystallization of both organic and inorganic materials, and helping to understand the early stages of cluster formation in metastable systems. Ongoing work is optimizing the implementation of the dual-detector system and refining the data handling and analysis methods. The experimental setup is designed to operate with a wide variety of sample environments including aerodynamic and acoustic levitators, host stages, capillaries and controlled humidity cells. With upgrades in synchrotron performance, beam quality and X-ray flux density, the ability to make time resolved (sub-second) in-situ ER-PDF measurements on bulk materials is now a realistic future research direction.

Declaration of competing interest

The authors declare that they have no known competing financial interests or personal relationships that could have appeared to influence the work reported in this paper.

CRediT authorship contribution statement

C.J. Benmore: Conceptualization, Methodology, Formal analysis, Investigation, Writing - original draft, Writing - review & editing, Supervision, Project administration. O.L.G. Alderman: Conceptualization, Methodology, Investigation, Writing - original draft. D. Robinson: Methodology. G. Jennings: Software. A. Tamalonis: Investigation. J. Ilavsky: Formal analysis. E. Clark: Investigation. E. Soignard: Software. J.L. Yarger: Software. J.K.R. Weber: Conceptualization, Methodology, Investigation, Resources, Writing - original draft, Supervision, Funding acquisition.

Acknowledgments

Thanks to Shinji Kohara and Charlie Weiss for useful discussions, Jim Rix for his advice with fabricating the large Kapton vacuum window. Thomas Bennett and Shichun Li are thanked for samples of ZIF-62 glass. This work was supported by the Advanced Photon Source, Argonne National Laboratory, USA, which is funded under U.S. DOE, BES, contract number DE-ACO2-06CH11357. OLGA, AT, EC and JKRW were supported under DOE, USA grant number DE-SC0015241. Professor Jeffery L. Yarger would like to acknowledge funding form the Department of Defense - Air Force Office of Scientific Research (DOD AFOSR, FA9550-17-1-0282),the Department of Defense - Army Research Office (DOD ARO, W911-NF19-10152) and the US National Science Foundation (NSF DMR BMAT Award # 1809645).

References

- [1] D.T. Bowron, A.K. Soper, K. Jones, S. Ansell, S. Birch, J. Norris, L. Perrott, D. Riedel, N.J. Rhodes, S.R. Wakefield, A. Botti, M.-A. Ricci, F. Grazzi, M. Zoppi, Rev. Sci. Instrum. 81 (2010) 033905.
- [2] S. Takata, J. Suzuki, T. Shinohara, T. Oku, T. Tominaga, K. Ohishi, H. Iwase, T. Nakatani, Y. Inamura, T. Ito, K. Suzuya, K. Aizawa, M. Arai, T. Otomo, M. Sugiyama, Proceedings of the 2nd International Symposium on Science at J-PARC Unlocking the Mysteries of Life, Matter and the Universe, J. Phys. Soc. Japan (2015).

- [3] S. Kohara, K. Ohara, H. Tajiri, C. Song, O. Sakata, T. Usuki, Y. Benino, A. Mizuno, A. Masuno, J.T. Okada, T. Ishikawa, S. Hosokawa, Z. Phys. Chem. 230 (2016) 339
- [4] J. Ilavsky, J. Appl. Crystallogr. 45 (2012) 324.
- [5] A.M. Beale, A.M.J. Van Der Eerden, S.D.M. Jacques, O. Leynaud, M.G. O'Brien, F. Meneau, S. Nikitenko, W. Bras, B.M. Weckhuysen, J. Am. Chem. Soc. 128 (2006) 12386.
- [6] N. Krins, J.D. Bass, B. Julián-López, P. Evrar, C. Boissière, L. Nicole, C. Sanchez, H. Amenitsch, D. Grosso, J. Mater. Chem. 21 (2011) 1139.
- [7] C. Boissiere, D. Grosso, H. Amenitsch, A. Gibaud, A. Coupé, N. Baccile, C. Sanchez, Chem. Commun. (2003) 2798.
- [8] M. Oversluizen, W. Bras, G.N. Greaves, S.M. Clark, J.M. Thomas, G. Sankar, B. Tilev, Nucl. Instrum. Methods Phys. Res. B 97 (1995) 184.
- [9] S.V. Ushakov, P.S. Maram, D. Kapush, A.J. Pavlik, M. Fyhrie, L.C. Gallington, C.J. Benmore, R. Weber, J.C. Neuefeind, J.W. McMurray, A. Navrotsky, Adv. Appl. Ceram. 117 (2018) 82s.
- [10] C.J. Benmore, J.K.R. Weber, Adv. Phys. X 2 (2017) 717.
- [11] X. Qiu, J.W. Thompson, S.J.L. Billinge, J. Appl. Crystallogr. 37 (2004) 678.
- [12] C.L. Farrow, S.J.L. Billinge, Acta Crystallogr. A 65 (2009) 232.
- [13] C.J. Benmore, Q. Mou, K.J. Benmore, D.S. Robinson, J. Neuefeind, J. Ilavsky, S.R. Byrn, J.L. Yarger, Thermochim, Acta 644 (2016) 1.
- [14] C.J. Benmore, ISRN Mater. Sci. 2012 (2012) 1.
- [15] O. Glatter, O. Kratky, Small Angle X-Ray Scattering, John Wiley & Sons, Ltd,
- [16] T. Narayanan, Soft Matter Characterization, Springer Netherlands, Dordrecht, 2008, pp. 899–952.
- [17] B. Hammouda, Probing Nanoscale Structures The SANS Toolbox. https://Www. Ncnr.Nist.Gov/Staff/Hammouda/The_SANS_toolbox.Pdf (n.d.).
- [18] A.C. Hannon, A. C., Nucl. Instrum. Methods Phys. Res. A 551 (2005) 88.
- [19] P.S. Salmon, R.A. Martin, P.E. Mason, G.J. Cuello, Nature 435 (2005) 75.
- [20] A.C. Wright, J. Non-Cryst. Solids 179 (1994) 84.
- [21] P.B. Moore, J. Appl. Crystallogr. 13 (1980) 168.
- [22] A.H. Narten, J. Chem. Phys. 56 (1972) 1905.
- [23] D.A. Keen, J. Appl. Crystallogr. 34 (2001) 172.[24] T.E. Faber, J.M. Ziman, Phil. Mag. 11 (1965) 153.
- [25] A.C. Hannon, W.S. Howells, A.K. Soper, Inst. Phys. Conf. Ser. (1990) 193-211.
- [26] C.G. Windsor, Pulsed Neutron Scattering, Taylor & Francis, 1981.
- [27] S.R. Elliott, J. Phys.: Condens. Matter 4 (1992) 7661.
- [28] L.B. Skinner, S.R. Chae, C.J. Benmore, H.R. Wenk, P.J.M. Monteiro, Phys. Rev. Lett. 104 (2010) 195502.
- [29] D.I. Svergun, M.H.J. Koch, Rep. Progr. Phys. 66 (2003) 1735.
- [30] L.B. Skinner, C.J. Benmore, J.B. Parise, Nucl. Instrum. Methods Phys. Res. A 662 (2012) 61.
- [31] A.P. Hammersley, J. Appl. Crystallogr. 49 (2016) 646.
- [32] C.A. Schneider, W.S. Rasband, K.W. Eliceiri, Nature Methods 9 (2012) 671.
- [33] G. Jennings, QXRD Readout Software for Flat Panel X-ray Detectors. http://Qxrd.Sourceforge.Net/Index.Html (n.d.).
- [34] Certified Scientifc Software, User Manual 1 (2017).
- [35] C.J. Benmore, J.K.R. Weber, M.C. Wilding, J. Du, J.B. Parise, Phys. Rev. B 82 (2010) 224202.
- [36] M. Wilding, C. Benmore, R. Weber, O. Alderman, A. Tamalonis, P.F. McMillan, M. Wilson, M. Ribiero, J. Parise, J. Non-Cryst. Solids X 3 (2019) 100027.
- [37] A.K. Soper, E.R. Barney, J. Appl. Crystallogr. 44 (2011) 714.
- [38] F. Marlton, O. Ivashko, M. v. Zimmerman, O. Gutowski, A.-C. Dippel, M.R.V. Jørgensen, IUCr, J. Appl. Crystallogr. 52 (2019) 1072.
- [39] J. Zaleski, G. Wu, P. Coppens, IUCr, J. Appl. Crystallogr. 31 (1998) 302.
- [40] F. Zhang, J. Ilavsky, G.G. Long, J.P.G. Quintana, A.J. Allen, P.R. Jemian, Metall. Mater. Trans. A 41 (2010) 1151.
- [41] A.J. Allen, F. Zhang, R.J. Kline, W.F. Guthrie, J. Ilavsky, J. Appl. Crystallogr. 50 (2017) 462.
- [42] A.K. Soper, E.R. Barney, J. Appl. Crystallogr. 45 (2012) 1314.
- [43] E. Lorch, J. Phys. C: Solid State Phys. 2 (1969) 305.
- [44] L.B. Skinner, C. Huang, D. Schlesinger, L.G.M. Pettersson, A. Nilsson, C.J. Benmore, J. Chem. Phys. 138 (2013) 074506.
- [45] O.A. Williams, Diam. Relat. Mater. 20 (2011) 621.
- [46] G. Fritz-Popovski, A. Bergmann, O. Glatter, Phys. Chem. Chem. Phys. 13 (2011) 5872.
- [47] M. Zienkiewicz-Strzałka, M. Skibińska, S. Pikus, Nucl. Instrum. Methods Phys. Res. B 411 (2017) 72.
- [48] T.D. Bennett, Y. Yue, P. Li, A. Qiao, H. Tao, N.G. Greaves, T. Richards, G.I. Lampronti, S.A.T. Redfern, F. Blanc, O.K. Farha, J.T. Hupp, A.K. Cheetham, D.A. Keen, J. Am. Chem. Soc. 138 (2016) 3484.